Available online at www.sciencedirect.com
ScienceDirect
Continental Shelf Research 27 (2007) 375–399
CONTINENTAL SHELF RESEARCH
www.elsevier.com/locate/csr

Observations and modeling of wave-supported sediment gravity flows on the Po prodelta and comparison to prior observations from the Eel shelf

P. Traykovski[a,*], P.L. Wiberg[b], W.R. Geyer[a]

[a]*Applied Ocean Physics and Engineering Department, Woods Hole Oceanographic Institution, Woods Hole, MA 02543, USA*
[b]*Department of Environmental Sciences, University of Virginia, Charlottesville, VA 22904, USA*

Received 13 January 2005; received in revised form 15 July 2005; accepted 20 July 2005
Available online 8 January 2007

Abstract

A mooring and tripod array was deployed from the fall of 2002 through the spring of 2003 on the Po prodelta to measure sediment transport processes associated with sediment delivered from the Po River. Observations on the prodelta revealed wave-supported gravity flows of high concentration mud suspensions that are dynamically and kinematically similar to those observed on the Eel shelf [Traykovski, P., Geyer, W.R., Irish, J.D., Lynch, J.F., 2000. The role of wave-induced density-driven fluid mud flows for cross-shelf transport on the Eel River continental shelf. Continental Shelf Research 20, 2113–2140]. Due to the dynamic similarity between the two sites, a simple one-dimensional (1D) across-shelf model with the appropriate bottom boundary condition was used to examine fluxes associated with this transport mechanism at both locations. To calculate the sediment concentrations associated with the wave-dominated and wave-current resuspension, a bottom boundary condition using a reference concentration was combined with an "active layer" formulation to limit the amount of sediment in suspension. Whereas the wave-supported gravity flow mechanism dominated the transport on the Eel shelf, on the Po prodelta flux due to this mechanism is equal in magnitude to transport due to wave resuspension and wind-forced mean currents in the cross-shore direction. Southward transport due to wave resuspension and wind forced mean currents move an order of magnitude more sediment along-shore than the down-slope flux associated wave-supported gravity flows.

Keywords: Po River; Adriatic Sea; Sediment transport; Turbidity currents; Fluid mud

1. Introduction

Wave-supported turbidity flows occur when high concentrations of sediment are suspended in the thin (1–10 cm) wave boundary layer with a sufficient density anomaly to enable down-slope gravitational forcing to dominate over other forcing mechanisms such as stress from the motion of the overlying water column. Recent observations and modeling have shown that these flows can be an important mode of cross-shelf sediment transport in areas with a substantial supply of fine sediment and high wave energy (Traykovski et al., 2000; Wright et al., 2001; Scully et al., 2002). Wave-supported turbidity flows

*Corresponding author. Tel.: +1 508 289 2638; fax: +1 508 457 2194.
E-mail address: ptraykovski@whoi.edu (P. Traykovski).

0278-4343/$ - see front matter © 2006 Elsevier Ltd. All rights reserved.
doi:10.1016/j.csr.2005.07.008

are effective in transporting recently delivered riverine sediment offshore, because they erode sediment in shallow water, where the wave energy at the seafloor and the supply of riverine fine sediment are both high, and they transport sediment down-slope into deeper water until the flow does not have enough wave energy to maintain the sediment in suspension. For given wave conditions, this provides a well-defined locus of deposition, since the depth where the suspension can no longer be maintained by wave energy can be determined by linear wave theory and a critical stress for resuspension. These flows are unlike "self-supporting" turbidity currents described previously in the literature (Middleton, 1993) in that these flows can occur on low angle slopes where the turbulence from wave energy is required to maintain the sediment in suspension. On steeper slopes, "self-supporting" turbidity currents can generate sufficient turbulence from their own motion to continue to suspend sediment and maintain the gravity flow in the absence of waves.

Based on seismic profiles from the California borderland basins, Moore (1969) was one of the first investigators to present a conceptual model for wave-supported turbidity flows. However, his suggestion that this could be an important mechanism to transport sediment from a riverine source to the mid- and outer-continental shelf was largely ignored until these flows were directly observed in the Eel River Strataform study on the northern California shelf (Traykovski et al., 2000; Hill et al., in press). On the Eel shelf, observations of the Eel River plume, boundary layer sediment transport processes, and the distribution of seafloor sediment properties revealed that wave-supported turbidity flows were the dominant mechanisms for creating mid-shelf flood deposits (Traykovski et al., 2000; Wheatcroft and Borgeld, 2000; Geyer et al., 2000; Hill et al., 2000). Tripod and hydrographic survey observations showed that the Eel River delivered sediment to the inner shelf and that wave-supported turbidity flows were responsible for transporting it to a depositional locus in 60–100 m water depths (Wheatcroft et al., 1996, 1997; Wheatcroft and Borgeld, 2000). Seafloor sampling studies on the Eel shelf showed that the flood deposits emplaced by wave-supported turbidity flow had a stratigraphic signature consisting of relativity thick deposits (5–15 cm) of terrigenous mud (Wheatcroft and Borgeld, 2000). Modeling of deposition due to wave-supported turbidity flows suggests that these flows could potentially establish a strong feedback mechanism with shelf morphology, and that this process could control the shape of the shelf-slope clinoforms (Friedrichs and Wright, 2004).

The EuroStrataform project was recently conducted on the northwestern coast of the Adriatic Sea to investigate the role of sediment transport processes on shelf stratigraphy and morphology in this environment (Nittrouer et al., 2004). In the northwestern Adriatic, the Po River supplies a large amount of sediment to the shelf during the fall and spring months, and there is both a rapidly growing delta (60–130 m/a; Bondesan, 2000) at the mouth of the Po and a clinoform along the shelf edge to the south of the delta. The drainage basin of the Po is much larger than that of the Eel. As a result, flood events on the Po last several weeks as opposed to several days for the Eel. Wave events at both sites have similar durations of one to several days due to wave generation by synoptic winds. However, the Adriatic has much smaller fetch than the Pacific Ocean, and the northwestern Adriatic is relatively shallow, thus the waves in the Adriatic have lower heights and shorter periods than those on the Eel shelf.

This paper discusses observations of wave-supported turbidity flows on the Po prodelta and compares them to the flows observed on the Eel shelf using dynamic force balances and a simple numerical model to predict the locus of deposition from these flows. The relative role of wave-supported turbidity current flux vs. along-shelf suspended sediment flux is also examined, as this may have important morphodynamic consequences regarding how much of the Po River sediment is preserved in the Po prodelta vs. how much is transported to the south. On the Eel shelf, the combination of a significant wave-supported turbidity flow flux and deposition combined with small net alongshore transport led to a spatially focused ("bulls-eye") depositional pattern with along-shelf scales of 40 km and across-shelf scales of 10 km. In contrast, on the western Adriatic Shelf there is a strong southward costal current (Artegiani et al., 1997) thus a preferential transport to the south was expected, which would lead to a net export of sediment from the region.

2. Site description and observational program

2.1. Site description

The Po River drains a 75,000 km^2 area of the southern Alps and the northern Apennine moun-

tains. It drains into the northwestern Adriatic via a 550 km^2 delta with five distributaries (Fig. 1). The main Pila distributary carries approximately 74% of the sediment load and the Tolle, Maistra, Donzella and Goro distributaries deliver 7%, 1%, 10%, and 8% of the sediment load, respectively (Nelson, 1970). Typical background flow rates in the Po River are around 1000 m^3/s, which increase to 5000–15,000 m^3/s during flood events. Annual sediment discharge has been estimated as 15 MT/year (Milliman and Meade, 1983), with exceptionally large individual flood events, such as the one in fall 2000, contributing amounts equal to the average annual load.

As part of the EuroStrataform project, several seafloor sampling cruises were conducted to measure the distribution of Po River sediment after flood events. Following the December 2000 flood, which had a peak discharge of 9650 m^3/s (the third largest flood discharge since 1918; Wheatcroft et al., 2006), the surveys documented flood deposits up to 36 cm thick in front of the Po distributaries (Palinkas et al., 2005, Wheatcroft et al., 2006). The offshore extent of these deposits was generally limited to water depths of less than 15 m; however, in certain locations the deposition extended into depths of 20–30 m. The sediment in these deposits was primarily fine silt and clay with a median grain size of 7–8 phi (4–8 μm) and a standard deviation of ~2 phi, i.e., poorly sorted. Some wave activity occurred between the peak of the discharge event and the seafloor sampling cruise, thus it is not clear if these depositional patterns reflect direct delivery to the seafloor from the river plume or the combination of seafloor delivery and subsequent transport processes.

Water column surveys of suspended sediment particles conducted during low to medium flow

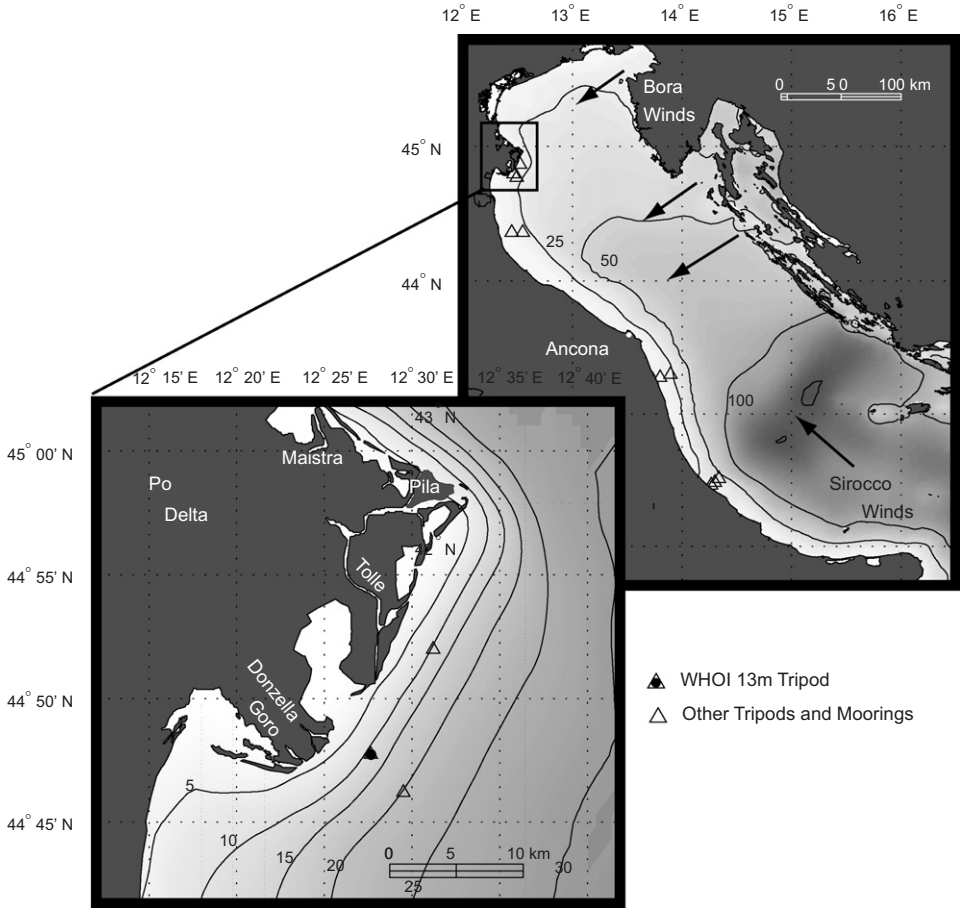

Fig. 1. Map of Adriatic and Po Delta (inset) showing distributaries and instrument locations. Contour depths are in meters and the arrows represent the regions of strong Bora winds due to mountainous topography on the northeastern Adriatic coast.

(1920 m^3/s) in June 2001 found sediment deposition directly in front of the Pila distributary in depths from 4 to 15 m (Fox et al., 2004). Two kilometers north and south of the Pila mouth, deposition occurred farther offshore (between 8 and 15 m) beyond the sand–mud transition located at 8 m. The seafloor became sandy again offshore of 25 m.

On the sub-aqueous prodelta, the seafloor slopes are relatively steep, with typical slopes of 0.002–0.003 in 10–20 m of water except directly in front of the main Pila distributary where slopes are approximately twice as steep. Beyond a depth of 25 m, the northern Adriatic seafloor becomes relatively flat, reaching maximum depths of 30–40 m. A thick deposit of Holocene sediment is present on the steep prodelta (Correggiari et al., 2001; Cattaneo et al., 2003). Immediately to the south of delta, the seafloor slopes become flatter, and the Holocene sediment deposit gradually thins over 50 km. In addition, a thick Holocene sediment deposit extends approximately 300 km along the western Adriatic coast (Trincardi et al., 1994). It has a clinoform structure with forset beds located between 20 and 50 m water depths.

2.2. Large-scale mooring array and tripod instrumentation

As part of the EuroStrataform project an array of instrumented surface moorings and tripods was deployed on the western Adriatic shelf to measure the modern transport processes that contribute to the formation of the Po delta and the shelf clinoforms to the south of Ancona. The array was deployed in early November 2002, recovered and redeployed in mid-February 2003, and recovered in late May of 2003. This paper focuses on data from a tripod located on the 13 m isobath in front of the Tolle distributary of the Po delta (Fig. 1), which returned good data for all but the last week of the second deployment. Another tripod was deployed further offshore, on the 22-m isobath, but it flipped over early in the first deployment and again halfway through the second deployment.

The tripods near the Tolle distributary had instrumentation to measure sediment resuspension, sediment flux, and the relevant oceanographic forcing processes. An upward looking 1.2 MHz ADCP measured the vertical structure of water velocity and backscattered acoustic intensity in 50 cm range bins starting 2.75 meters above bed (mab). The ADCP recorded averages every 30 min, resolving mean currents while averaging out wave velocities. Two Nortek Vector acoustic Doppler velocimeters (ADVs) with pressure sensors were located with sampling volumes 35 and 100 cm above the bottom of the tripod feet. A three-frequency (1.0, 2.5 and 5.0 MHz) acoustic backscattering system (ABS) was mounted with transducers 115 cm above the feet. These instruments measured acoustic backscatter in 128 1-cm range bins, and were used to estimate near-bed sediment concentration and changes in bed elevation relative to the tripod. The ADVs recorded 20-min bursts of 2 Hz samples every hour, thus sampling both wave and mean current processes. Optical backscattering sensors, which were located 40 and 100 cm above the feet, became compromised by biofouling relatively early in the deployment, and thus did not produce much useful data. Seabird conductivity, temperature and depth (CTD) sensors were mounted on both tripods and on a nearby surface mooring to measure density stratification associated with freshwater discharge from the Po.

The ABS bottom elevation data showed that the tripod on the 13 m isobath sank 25 cm into the seabed during the first storm, presumably due to scour around the footpads. The relative pressure difference between this tripod and the 22 m isobath tripod confirmed that this change was not an actual seabed elevation change. Thus, after the first storm the actual heights of the velocimeters were 10 and 75 cmab.

2.3. ABS and ADCP calibrations and flux estimates

The acoustic backscatter measurements were calibrated to quantify the relationship between backscatter and sediment concentration. The combined measurements from the ABS and ADCP generated a vertical profile of sediment concentration from the seafloor to 10 mab. In the upper 3 m of the water column, the scattering increased during storms, most likely due to bubble injection from whitecaps, thus these data were considered invalid. The ABS was calibrated in a recirculating tank with sediment from the upper 5 cm of a box core collected near the tripod on recovery. The range-dependence of the acoustic backscatter was corrected for spherical spreading, water attenuation, and sediment attenuation using the algorithms developed by Thorne et al. (1993), and Lee and Hanes (1995). At high concentrations (in excess of 10 g/l), the algorithms used to correct for sediment

attenuation were found not to converge at the two higher frequencies (2.5 and 5.0 MHz) as the acoustic energy was sufficiently attenuated to be below the dynamic range of the instrument. This problem did not occur with the 1.0 MHz sensor, making more accurate concentration estimates in the high concentration layers possible.

An ABS with 2.5 and 5.0 MHz transducers that was deployed in the Eel Strataform study also had problems with acoustic attenuation at high concentrations (Traykovski et al., 2000). As a result, suspended sediment in concentration in Traykovski et al. (2000) was assumed to be constant below the lutocline during periods of high acoustic attenuation. Here the lutocline is defined as the region of maximum concentration gradient at the top of the high concentration layer. The ABS on the 13-m Po tripod had a 1.0 MHz transducer as well as a 2.5 MHz transducer similar to that used in the Eel study, permitting re-examination of the concentration estimates from the Eel. Estimates of concentrations from the Po 2.5 MHz transducer, calculated using the same procedure as in the Eel, resulted in estimates of concentrations in the high concentration layers, where acoustic attenuation was significant, that were approximately a factor of two lower than the estimates from the 1.0 MHz transducer. This implies that the original concentration estimates for the thin, near-bed, high concentration layers found in the Eel study (Traykovski et al., 2000) were underestimated by a factor of two.

Because particle sizes in the bed are much smaller than the acoustic wavelengths of the ABS, the scattering is in the Raleigh regime with the ratio of acoustic intensity to sediment concentration having a size dependence of d^3, where d is particle diameter (Lynch et al., 1994), assuming the density of the particles is constant. Since all three ABS transducer frequencies are in the Raleigh regime, they are linearly dependent with respect to size at low concentrations where attenuation is insignificant (i.e. all three frequencies have a size dependence of d^3 with a different constant). This is superimposed on the theoretical linear relation between concentration and backscattered intensity for a fixed grain-size distribution once sediment attenuation has been accounted for. The suspensions of fine sediment offshore of the Po River, however, are dominated by flocs whose size and density is controlled by aggregation and disaggregation processes in the water column (Fox et al., 2004). While well-controlled acoustic calibration experiments with flocs have not yet been performed, a recent field calibration over a single tidal cycle in the Hudson estuary, where floc size variability was measured, gave typical errors of 10–25%, with a maximum error of 50%, in the relationship between acoustic intensity and sediment concentration (Traykovski et al., 2004). The calibration coefficients found in the tank calibration for Po sediment were similar to those found in the field calibration performed in the Hudson. The calibrated scattering data was able to explain 95% of the variance in the concentration estimates from bottle samples taken in the tank. However individual concentration estimates, particularly at low concentrations had errors of up to 50% of the concentration. Unfortunately, calibrations with in situ bottle samples from the field near the Po were not possible, as sediment samples were not taken during energetic, high concentration conditions.

To calibrate the relationship between the backscattered signal of the ADCP and sediment concentration, an additional step is required since the ADCP amplitude output minus system noise ($E-E_r$) is proportional to backscattered intensity in decibels with an unknown constant of proportionality (K_c). Thus, there is both a logarithmic calibration coefficient (K_c), and a linear calibration coefficient (C_0). The linear coefficient relates the range-corrected output to sediment concentration. Concentration can be found as (Eq. (5) from Deines, 1999):

$$C_V = C_0 + 20\log_{10}(R) - L_{DBM} - P_{DBW} + 2\alpha R + K_c(E - E_r). \quad (1)$$

In Eq. (1), R is the range from the transducer and the term involving $\log_{10}(R)$ compensates for spherical spreading. L_{DBM} and P_{PDM} represent transmit pulse length and transmit power, respectively. Background water attenuation is accounted for with the term $2\alpha R$, where α is the attenuation coefficient. The logarithmic constant of proportionality (K_c) was found by matching the dynamic range of the lowest range bin of C_v to an ABS range bin 30 cm from the ABS transducer (60 cmab). This method resulted in a K_c of 0.52, which is within the range of values (0.35–0.55 dB/Bit) found in Deines (1999). The linear calibration factor was found by combining C_0, L_{DBM}, and P_{DBW} into a single calibration coefficient and estimating this coefficient using the ABS data, by assuming that there are periods of vertically uniform background scattering

during low concentrations. This assumption also ensured that the concentration in the lowest bin of the ADCP data (2.75 mab) was never larger than the concentration in the ABS bin 50 cmab.

The ADCP and the ABS concentration estimates were merged into a single data set by interpolating between the upper ABS bins 60–70 cmab and the lower ADCP range bin at 2.75 mab. The interpolation was performed by transforming the vertical coordinate into log space, and fitting the intensity data with cubic splines (performed using the MATLAB^{TM} spline toolbox) that matched the data and the first derivative of the data at the end points. A similar procedure was employed to merge the ADCP velocity data with the ADV velocities closer to the bed. The transformation of the vertical coordinate into log space was performed so that linear fits would produce a logarithmic boundary profile consistent with ''law of the wall.'' Since the ADV measures velocities at single point, and not a velocity profile, the cubic splines in log vertical coordinates were fit to the ADCP data, the first derivative of the ADCP data closest to the seafloor, the ADV data at 75 and 10 cmab, and a seabed boundary condition. The seabed boundary condition constrained the velocity to be zero at a height of $z_0 = 0.056$ cm, consistent with a coefficient of drag of 0.003 (i.e. $C_d = (\kappa/\log(z/z_0))^2$, where $\kappa = 0.41$, and $z = 1.0$ m). The velocity and concentration profiles were multiplied to estimate flux profiles from the seabed up to 10 m above the seabed. The errors in this flux estimate are much more likely to be due to the concentration estimate than the velocity estimate. As stated previously the ABS calibration has errors of ~10–50%. In addition, there are poorly quantified errors in using the ABS to estimate the calibration coefficients for the ADCP, and potential errors could result from interpolating the concentration data from 0.6 to 2.5 mab. However, this flux profile estimate does provide a method to compare near bed transport processes, such as the wave-supported gravity flows and larger vertical scale wave resuspension-mean current transport processes that would be inadequately sampled using the ABS data alone.

3. Results

3.1. Forcing conditions

During the fall 2002–spring 2003 instrument deployment on the northwestern Adriatic shelf, the Po River had a flood event with a 7960 m^3/s peak flow that was above flood stage (>7000 m^3/s) for 6 days, and above background flow (>2000 m^3/s) for over 1 month (11/17/2002–12/24/2002, Fig. 2(a)). The largest waves of the deployment (3.8 m significant wave height) occurred immediately before this period of elevated river discharge (11/15/2003–11/17/2003; event HC1 in Fig. 2, where the HC signifies events with high sediment concentration near-bed layers). These waves were generated by Sirocco winds from the southeast, which generate swell that propagates from the central Adriatic towards the northwestern Adriatic (Sherwood et al., 2004). During the period of high river discharge, there were two intervals with significant wave heights over 1.5 m (Fig. 2; events labeled HC2 and HC3). The first of these wave events (HC2) was also forced by Sirocco winds while the second (HC3) was forced by Bora winds from the northeast. Bora winds usually generate shorter period waves than the Sirocco swells from the southeast, owing to the limited fetch to the northeast of the study site. Typical peak wave periods for the two Sirocco events were 8–9 s; the Bora event had typical periods of 6–8 s. Later in the winter, once the Po has returned to discharges slightly above background flow, there were several wave events over 1.5 m significant wave height that were forced by Bora wind conditions (Fig. 2, events labeled DS1 through DS4, where DS signifies events with dilute suspensions (DSs) as opposed to the high concentration events). These wave heights are typical winter conditions for the Northwestern Adriatic based on wave buoy data from Ancona.

3.2. Sediment concentration profiles during high concentration and DS events

During the wave event before river discharge began to rise (HC1) and during wave events coinciding with the elevated river flow (HC2 and HC3), there were thin, high suspended sediment concentration layers with thicknesses of ~5–8 cm above the seafloor. These layers had near-bed concentrations of 10–50 g/l, which decreased to 0.2–3 g/l at 10 cmab and 0.02–0.05 g/l at 1 mab (Fig. 3(a)). Thus 80–95% of the suspended sediment mass was located within the lower 10 cm of the water column for these profiles. In contrast, the sediment concentration profiles during the DS events (DS1–DS4), when the river discharge had returned to almost background levels, were much

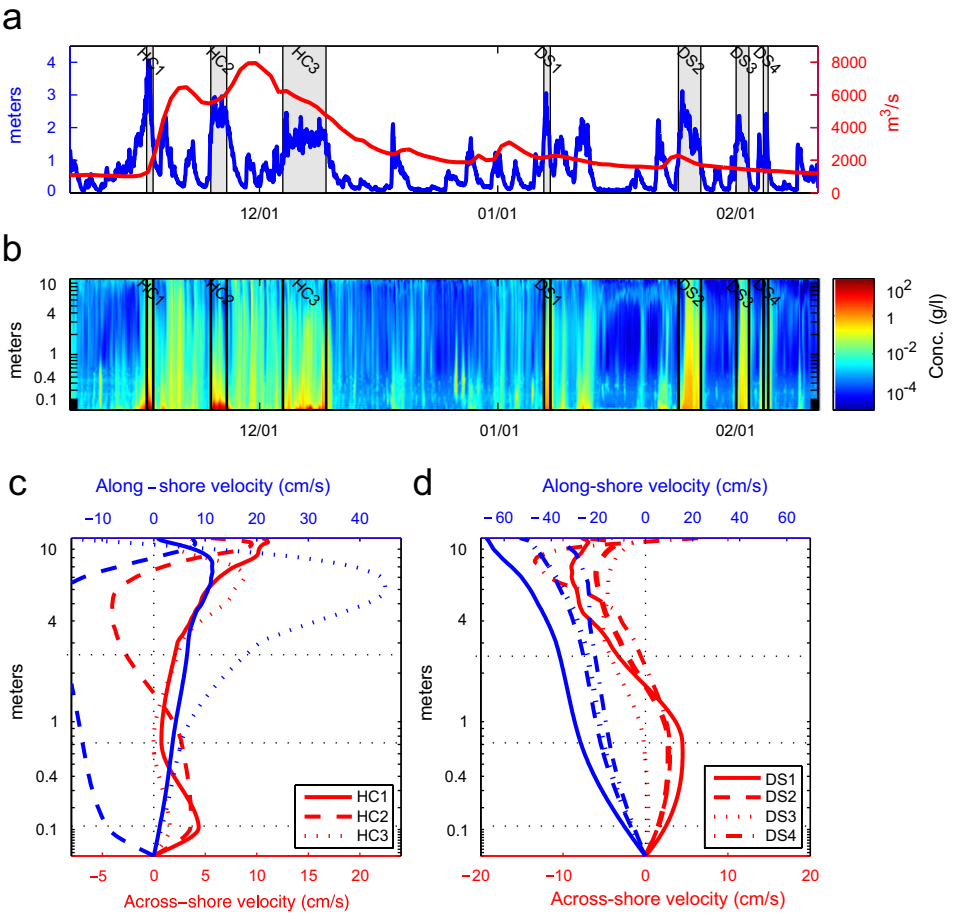

Fig. 2. Time series of: (a) Significant wave Height and Po River discharge; (b) ABS/ADCP measured sediment concentration profiles, with velocity profiles showing (c) high concentration events (HC1–HC3) and (d) dilute suspension events (DS1–DS4). The two lower horizontal dashed lines in panels c and d show the location of the Nortek Velocimeter sampling volumes. The upper dashed horizontal line indicates the lowest bin of the ADCP data. Profiles are averaged over the entire event as denoted by the vertical lines and shaded areas in panels a and b. Blue lines (referenced to upper x-axis) represent along-shore flows and red lines (referenced to lower x-axis) represent across-shore flows. Offshore and north are both positive on the x-axis. The near-bed offshore flow associated with the high concentration events is visible in panel c. This is contrasted to the thicker boundary layers shown in panel d.

lower near the seafloor (0.5–2 g/l), and did not decay as quickly in the vertical (0.2–0.8 g/l at 10 cmab and 0.07–0.1 g/l at 1 mab). In these profiles, 50% of the sediment mass was located below 1–2 mab, and 85% of the sediment mass was located below 4–6 mab.

3.3. *Velocity and flux profiles during high concentration wave-supported turbidity flows events*

The across-shore velocity profiles for events HC1–HC3 (Fig. 2) show a jet of offshore flow as measured by the lower velocimeter at 10 cmab, with weaker offshore flow above it. This is in contrast to across-shore velocity profiles taken at other times, and alongshore profiles taken at all times, which exhibit monotonically increasing flow from the seafloor to the height of the upper velocimeter at 75 cmab, consistent with frictional drag on the seafloor and a mean current boundary layer that is approximately 1 m thick. The offshore flows in the lower 10 cm of the water column during periods when high concentration layers were present are characteristic of wave-supported turbidity flows as observed on the Eel shelf (Traykovski et al., 2000). The down-slope (offshore) velocity observed at the top of the high concentration layer was due to the

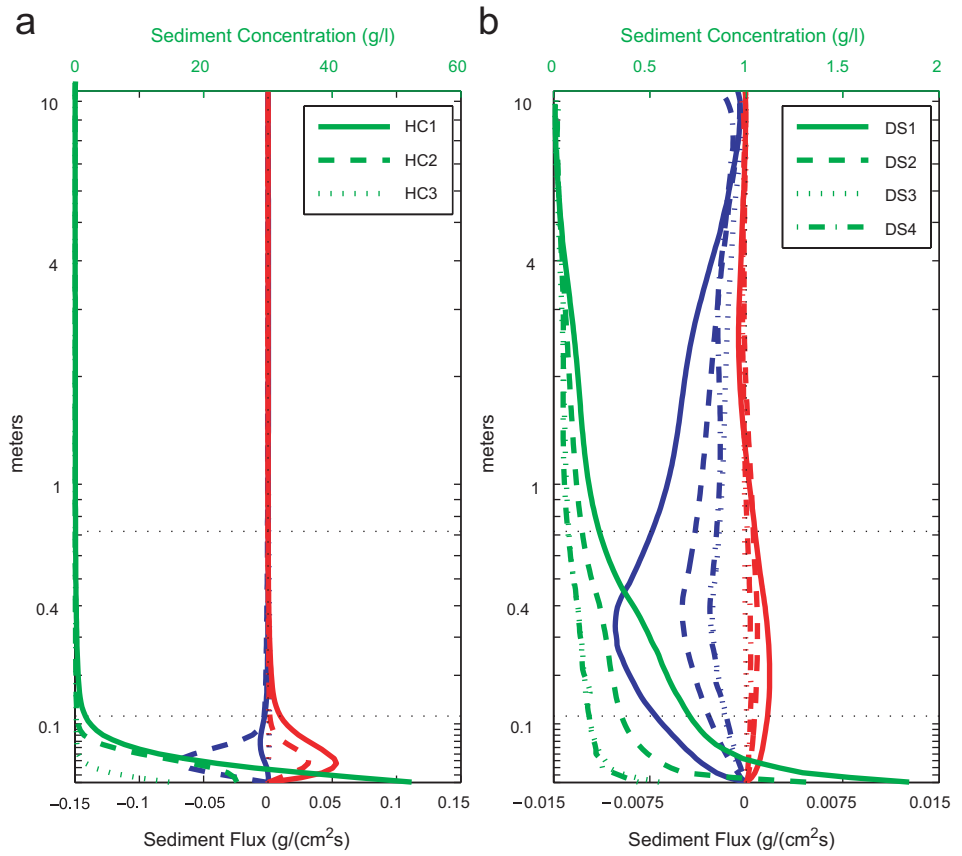

Fig. 3. Profiles of flux (red lines for across-shelf fluxes and blue lines for along-shelf fluxes), and concentration (green lines) for (a) high concentration and (b) dilute suspension events. Profiles were averaged over the entire event as indicated by gray shaded areas in Fig. 2a. Positive on the x-axis is offshore and north.

high density of the high concentration layer relative to the ambient seawater. The high excess density combined with a sloping seafloor led to down-slope flow. The details of the shape of the velocity profile may not be accurate because the velocity was interpolated between sensor locations, but the profile is constrained at the sensor heights and at the seabed. The upper parts of the across-shore velocity profiles during the high concentration events displayed more variability. They generally had offshore flow near the surface, but some of the profiles had onshore flow in the mid-water column. The along-shore velocity profiles during events HC1–HC3 also displayed considerable variability that does not appear to correlate with wind forcing. The two velocity profiles (HC1 and HC2) that were taken during Sirocco winds show northward and southward velocities in the mid-water column, respectively. The profile (HC3) taken during Bora conditions shows northward mid-water column flow with a southward near surface layer (Fig. 2).

Across-shelf suspended sediment flux profiles from the wave-supported turbidity flow events (Fig. 3(a)) had maxima 4 cmab; 50% of across-shelf flux occurred below 5–8 cmab, and 85% of across-shelf flux for event HC1 occurred within 20 cmab owing to the high concentrations in the lower 10 cm. Events HC1–HC3 transported 42, 33 and 18 kg/cm offshore, respectively. Event HC2 had a larger near-bed alongshore (southeastward) component of flux (80 kg/cm) than the near-bed across-shore component, due to forcing of the near-bed high concentration layer from overlying currents. Event HC3 had an along-shore (northwestward) flux of 98 kg/cm, primarily due to transport in the mean current boundary layer. In event HC3 there were three periods when mean currents increased to 30–40 cm/s and were able to mix several hundred mg/l of suspended sediment (measured 50 cmab) up out of the high concentration layer, where it was transported by the northwestward mean currents. When the mean current decreased below 15–20 cm/s, the

suspended sediment was trapped within the high concentration layer, which maintained concentrations of 10–20 g/l, while the concentrations 1 mab decreased to tens of mg/l. Although events HC1–HC3 all had high concentration layers near the seafloor, it was only during event HC1 that the flux was dominated by the gravitational flow of this layer. In event HC3, the flux was dominated by transport above the high concentration layer.

3.4. Velocity and flux profiles during DS downcoast transport events

During the DS events after the Po had returned to near background discharge, the vertical profiles of velocity show remarkable consistency in structure, with some variability in magnitude (Fig. 2, events DS1–DS4). During this period, a well-defined southward coastal current became established in the northwestern Adriatic. The across-shore velocity profiles show onshore flow in the upper portion of the water column and offshore flow in the lower portion of water column. The along-shore velocity profiles show strong southward flow at the surface (up to 70 cm/s), which monotonically decreases toward the seafloor. Both the along- and across-shelf profiles of measured velocity indicate the presence of a frictional bottom boundary layer at least 75 cm thick. This vertical structure of the along and across-shore velocity components is consistent with a thermal wind balance during downwelling-favorable conditions.

In contrast to the wave-dominated high concentration events, the Bora wind forced DS events had sediment flux that occurred higher in the water column (Fig. 3(b)) and transported an order of magnitude more sediment in the along-shore direction than in the across-shore direction. They were typically characterized by stronger mean current, with velocities of 35–70 cm/s as opposed to 0–20 cm/s for events HC1 and HC2. Alongshore flux maxima occurred 30–40 cmab; 50% of the flux was below 2–4 m, as opposed to 5–8 cmab for the high concentration events, and 85% of the flux was below 5–7 mab. Events DS1 through DS4 transported 217, 476, 168, and 115 kg/cm alongshore to the southeast and 10.5, 4.8, 17.1 and 14.8 kg/cm onshore, respectively. Although there was offshore flow of ~1–5 cm/s in the bottom boundary layer during the DS events, and the sediment concentrations were highest near the bed, stronger onshore flow above 2 mab resulted in net onshore flux. The sediment was vertically distributed in the water column so that ~35–50% of the mass was above the velocity reversal. Coupled with higher flow velocities in the mid-water column, this leads to onshore fluxes during DS events. These onshore fluxes were comparable in magnitude to the offshore fluxes that occurred during the wave-supported gravity flow events, and thus the seasonally integrated across-shore transport was small (Fig. 4(c)). The across-shore fluxes were an order of magnitude smaller than the alongshore fluxes to the southeast associated with Bora wind forcing for these events.

3.5. Seasonal time-scale fluxes

In order to examine the relative contributions of variations in velocity and sediment concentration to the seasonal time-scale fluxes, flux-weighted depth integrals of sediment concentration were calculated. Flux-weighted integral were calculated because the depth averaged concentration or single elevation concentration values can be substantially different from the concentration in the layer that contributes to the flux. The flux profiles $q(z)$ were used to estimate flux-weighted vertical integrals of sediment concentration C_q:

$$C_q = \int c(z)q(z)\,\mathrm{d}z \Big/ \int q(z)\,\mathrm{d}z. \tag{2}$$

The depth integrals were evaluated from 1 cmab to 10 mab. Flux-weighted integrals of velocity were also calculated, but these were found to be similar to velocities at 75 cmab, thus velocities from the ADV at 75 cmab are shown in Fig. 4(b). The velocity time series shown in Fig. 4(b) were low-pass filtered to remove 5–10 cm/s tidal flows. The HC events had concentrations C_q of ~10 g/l and offshore velocities of 5–10 cm/s (Fig. 4(b)). In terms of the contribution to the seasonal flux over the winter 2002–2003, the three wave-supported turbidity flow events combined transported 80 kg/cm offshore. This was largely compensated by the onshore transport during the DS events (DS1–DS6), thus the total across-shore transport was 20 kg/cm offshore (Fig. 4(c)). The DS events had concentrations C_q of 0.2–0.4 g/l and downcoast (southward) velocities U_q of 20–35 cm/s. While there was some upcoast transport during two of the high concentration events, the dominant transport mechanism was downcoast transport due to Bora forcing. The five major Bora events transported 1200 kg/cm

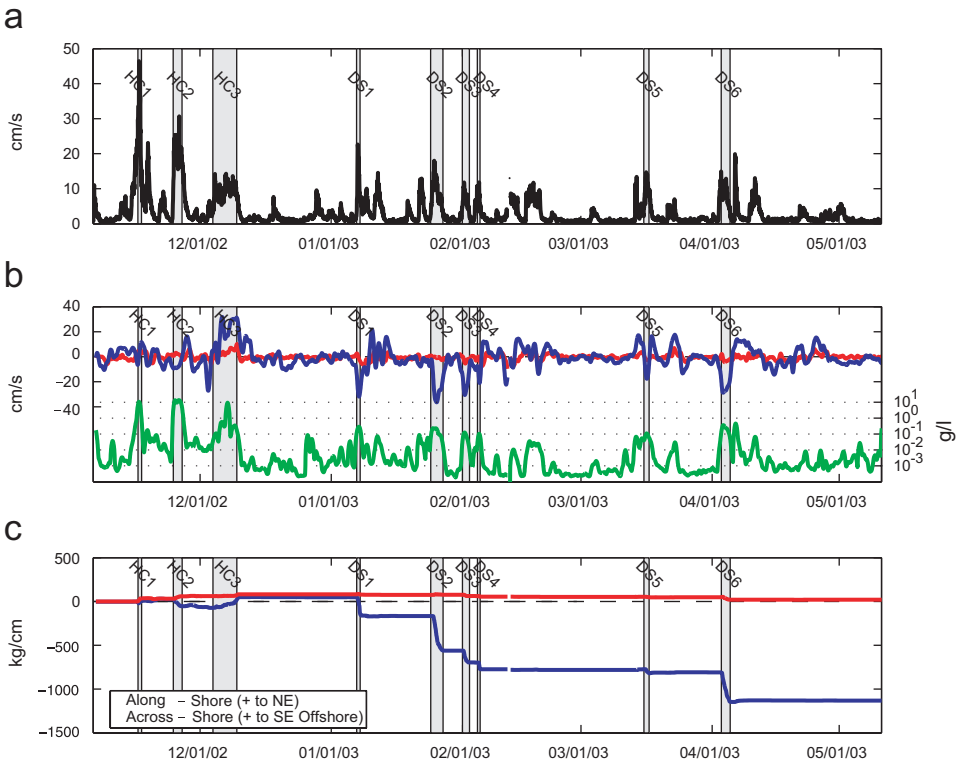

Fig. 4. (a) Representative wave-velocity time series; (b) mean currents from the ADV at 75 cmab (red for across-shelf and blue for along-shelf) and flux-weighted depth-averaged concentration (green) time series; and (c) cumulative depth integrated flux time series (red for across-shelf and blue for along-shelf) for first and second deployments.

downcoast from November 2002 to May 2003. Most (75%) of this transport occurred during four events in January 2003, and the first week of February. A final Bora event in first week of April accounted for the remaining 25%.

4. Modeling of sediment concentration using a 1D vertical model

4.1. Forcing conditions

In order to understand the relative magnitudes of the Bora-forced downcoast transport events (DS events) compared to the across-shore, wave-supported turbidity flow events (HC events), the details of the sediment transport processes are examined for each type of event. One of the primary differences in these two types of events is in the physical oceanographic forcing conditions. Bora conditions have strong NE winds in the northern Adriatic, which when combined with fresh water from the Po, result in a strong downcoast flow. In contrast, during Sirocco events the SE wind is typically strongest in the southern part of the Adriatic, thus strong currents are not generated near the Po delta. However, Sirocco winds do create large swells that travel directly towards the SE facing southern side of the Po delta. The largest waves of the observational period occurred during the Sirocco-forced event HC1 (Figs. 2 and 3). The second wave-supported turbidity flow event (HC2) event also occurred during Sirocco conditions and coincided with a period of high Po River discharge, thus potentially creating a source of easily resuspended sediment ideal for creating high concentration near-bed suspensions. The third wave-supported turbidity flow event (HC3) occurred during Bora conditions, and although it had a high concentration near-bed layer, the flux was dominated by transport higher in the water column thus showing many of the characteristics of a DS event. All the events classified as DS events did not have a near-bed high concentration layer, and occurred during Bora conditions.

4.2. Sediment concentration bottom boundary condition

To examine sediment resuspension in response to the oceanographic forcing, bed shear stress was calculated using a 1D bottom boundary layer model (Wiberg and Smith, 1983; Wiberg et al., 1994). This model calculates wave friction velocity (u_{*w}), mean current friction velocity, (u_{*c}), and the non-linear combined wave–current friction velocity (u_{*cw}). Since the bed near the tripod location consisted primarily of clay and silt-sized sediment, and seafloor ripples are not expected to form, the bed roughness was set to $z_0 = 0.056$ cm to be consistent with a canonical drag coefficient of $C_d = 0.003$ referenced to 1 mab. The model calculates an eddy viscosity profile proportional to $u_{*cw}z$ in the wave boundary layer and $u_{*c}z$ in the mean current boundary layer. Each near-bed linear segment decays smoothly in the vertical with an exponential scaling factor as described in Wiberg and Smith (1983). The inputs into the model are: mean currents $(\bar{u}, \bar{v})$ (from 75 cmab as shown in Fig. 4(b)), radian wave frequency (ω_r) and significant wave velocity calculated from the Nortek Vector data at 75 cm as $u_{bsig} = 2\sqrt{(u_{rms}^2 + v_{rms}^2)}$ (Fig. 4(a)), where the root mean square (*rms*) velocities were recalculated over frequencies from 0.02 to 0.20 Hz so as to only include wave band variations (Fig. 4(a)). Representative wave velocities ($u_{br} = u_{bsig}/\sqrt{2}$) are often used in boundary layer calculations (e.g., Madsen et al., 1994), thus u_{br} is plotted in Fig. 4. Representative radian wave frequency (ω_r) was calculated as the variance-weighted spectral mean as described in Madsen (1994). Wave direction was calculated as the direction of the peak of the wave spectrum. While the model calculates wave stress from a solution to the wave boundary layer velocity profiles using its eddy viscosity profile, the wave stress produced by the model can be approximated as

$$\tau_w = \tfrac{1}{2}\rho_w f_w u_{br}^2 \tag{3}$$

with

$$f_w = 0.04(u_{bsig}/\omega_r k_n)^{-0.025} \tag{4}$$

where f_w is the wave friction factor, ρ_w is water density and the roughness scale $k_n = 30z_0$ (Fredsøe and Deigaard, 1992).

Wave stress was the dominant contributor to the combined stress. This is typical for continental shelf environments with roughly equal current and wave speeds owing to the higher shear in the thin (order of centimeters) wave boundary layer compared to the thicker (order of meters) mean current boundary layer. In the first two high concentration events, the current stress contributed no more than 5% of the combined stress. In the third high concentration event and the DS events, the current stress contributed 5–30% of the combined stress at the seafloor.

For the sediment transport calculations, we used the grain-size distribution shown in Table 1, which is based on surface (0–2 cm) grain-size distributions from a nearby core. The sediment characteristics of the bed were assumed to be uniform with depth in the bed. Critical shear stresses (τ_{cr}) were calculated from Shields curve (Miller et al., 1977) and settling velocities, w_s, were calculated using Dietrich's (1983) relationships. For sediment grain sizes with $\tau_{cr} < 0.1$ Pa based on Shields curve, a canonical τ_{cr} value for fine sediment of 0.1 Pa was used. This was consistent with the ABS near bed data and was consistent with analysis of erosion chamber data from a core taken near the tripod in February, 2003 (Stevens et al., 2007). Similarly, for sediment grain sizes with $w_s < 0.1$ cm/s based on Dietrich's (1983) relationships, a typical flocculated settling velocity for fine sediment of $w_s = 0.1$ cm/s was used. A sediment reference concentration bottom boundary condition of

$$c_r = \frac{c_b \gamma_0 S_{sfm}}{1 + \gamma_0 S_{sfm}} \tag{5}$$

was used to calculate sediment concentration at z_r, where $S_{sfm} = \tau_{cw}/\tau_{cr} - 1$, $c_b = 0.2$ (based on an average porosity of roughly 80% measured in the surface layer of the core) and $\gamma_0 = 0.002$. The reference height (z_r) was set to 3 times the average grain diameter.

The modeled reference concentration was compared to the near bed ($z = 1$–2 cmab) concentration from the ABS data (Fig. 5). For the three major wave events associated with high concentration events, Eq. (5) agrees relatively well with the data. Some of the smaller peaks in wave stress between

Table 1
Model input sediment properties

Size (∅)	τ_{cr} (Pa)	Settling velocity, w_s (cm/s)	Bed fraction
8.0	0.1	0.1	0.378
6.0	0.1	0.1	0.463
4.0	0.1	0.228	0.123
2.0	0.19	2.264	0.036

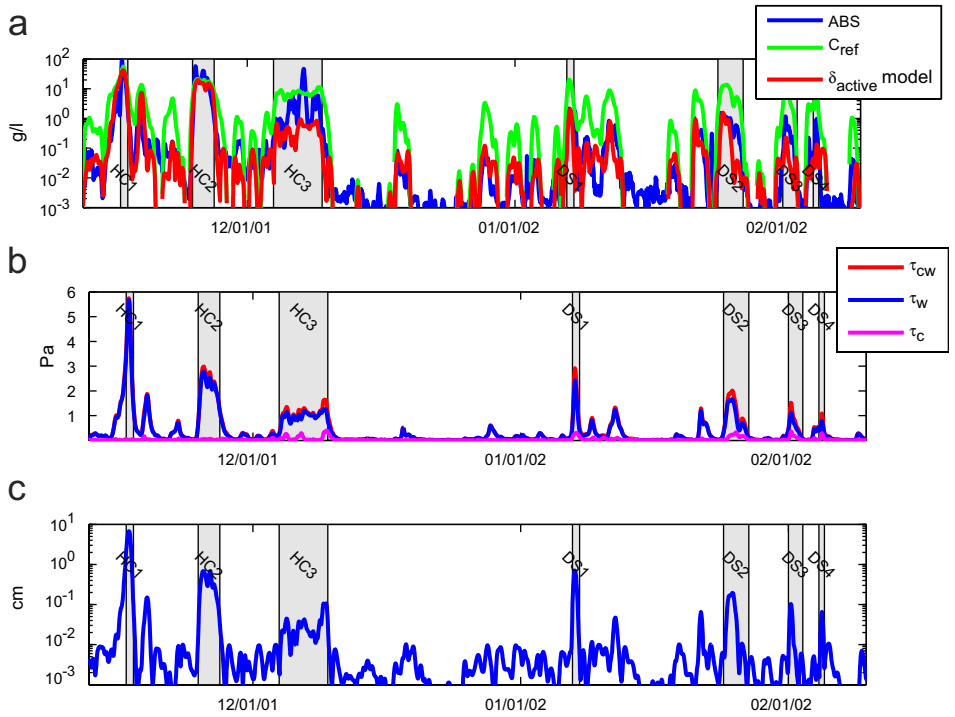

Fig. 5. (a) ABS near-bed concentration time series with reference concentration model predictions and active layer model predictions. (b) Wave (τ_w), current (τ_c) and combined wave–current (τ_{cw}) shear stress time series. (c) Active layer depth (δ_{active}) time series.

the three large wave events are not well predicted, as the model gives an order of magnitude more near bed sediment than the data indicate. Following the high concentration events, when the Po discharge is reduced, Eq. (5) consistently overpredicts the near bed concentration by an order of magnitude. One possible explanation for the good agreement during the high concentration events and over prediction during the Bora-forced DS events would be the presence of a layer of easily resuspendable sediment during the high concentration events. The wave-supported turbidity events could have transported enough of this easily resuspendable sediment offshore so that a more erosion-resistant bed was left for the subsequent Bora-forced DS events. One problem with this explanation is that a high concentration layer was observed during the first large wave event (HC1), which occurred just *before* the Po flood. This was the first large wave event of the fall/winter season, and the Po had some minor discharge peaks ($\sim$3000 m^3/s) earlier in the year. Thus the accumulated deposition from these discharge events, combined with the fact that this was the first major storm of the fall, may have also resulted in a supply of easily resuspended sediment for this event. However, this sediment would have had ample time to consolidate before the large wave events in November.

An alternative formulation to Eq. (5) for the bottom boundary conditions for suspended sediment concentration is to specify an erosion rate. This is commonly used for fine-grained, cohesive sediments and can capture the increase in critical shear stress with depth that generally characterizes consolidated, muddy beds. As part of the EuroStrataform program, erosion chamber measurements were made on cores taken near the 13 m tripod (Fig. 1) during the mid-February turn-around cruise to determine the amount of sediment that could be eroded at a given stress (Stevens et al., 2007). The results indicate that resuspension at the 13-m tripod site was limited by sediment availability, which is controlled by the rate of increase of critical shear stress with depth in the bed. Therefore, the bottom boundary condition can be specified by limiting the amount of sediment in suspension to that available in the layer whose thickness (δ_{active}) is set by the depth where the critical shear stress is equal to the wave–current shear stress.

Cumulative mass eroded as a function of shear stress was measured for two cores from the 13-m tripod site. One was tested immediately upon retrieving the core while the other was tested 5 h later. Mass eroded was converted to depth using a porosity of 0.8, consistent with Eq. (5) (Fig. 6). The difference between the results for the two cores could be a product of local variability in seabed properties or the result of consolidation of the core that remained on deck related to vibrations that were present when the ship was moving. Unfortunately, the erosion chamber apparatus was only able to support stresses up to 0.4 Pa, while the large wave events in the field had stresses of 1–6 Pa. Thus using the erosion measurements to predict field measurements during storms requires extrapolating to higher stresses. Using either of the curves fit (solid or dotted line in Fig. 6) to the erosional chamber measurements to determine the near-bed concentration time series results in a reasonable fit for the DS events with shear stresses from 1.0 to 2.5 Pa and the low stress events (for example the two small events between HC3 and DS1 with stresses ~0.5 Pa and near bed concentrations of ~0.1 g/l). However, using the curve fit to the erosion chamber measurements under-estimates concentrations during the high stress events at the beginning of the record (HC1 with $\tau_{cw} = 5.7$ Pa and approximately 100 g/l peak near-bed concentration and HC2) by an order of magnitude. In order to model both the moderate and high shear stress events successfully, a more rapid increase of δ_{active} with respect to stress is required in the region from 2.0 to 6 Pa. Thus, the near bed ABS concentration time series, including both high and moderate stress events, was reasonably fit (Fig. 5(a), time series denoted δ_{active} model) using an active layer depth of:

$$\delta_{active} = \begin{cases} (1/c_b\rho_s)0.05\tau_{cw}^{1.24}, & \tau_{cw} < 2.25\,\text{Pa}, \\ (1/c_b\rho_s)0.08\tau_{cw}^{3.5}, & \tau_{cw} \geqslant 2.25\,\text{Pa} \end{cases} \quad (6)$$

with τ_{cw} in units of Pascals and δ_{mix} in centimeters. Eq (6) represents a combination of the fit to the erosion chamber (dotted line fit to squares in Fig. 6) measurements, and a steeper curve to match the ABS near-bed concentration data (dashed line in Fig. 6). The ABS data do not constrain the active layer depth at shear stresses lower than 0.1 Pa as the concentrations at these low shear stresses are too small to be accurately measured by the ABS.

There are several possible explanations for the disagreement between the erosion chamber results and the active layer depth required to match the field data at high stresses. First, bed consolidation is time-dependent. When the Po was actively supplying sediment to the prodelta, there may have been a relatively unconsolidated layer of sediment present at the bed surface, that later consolidated to at least the degree that was observed in the erosion chamber measurements. Alternatively, if the bed was similar throughout the deployment to the bed sampled in February, the dramatic increase in sediment availability required to predict the high concentration events may be reflective of a bed fluidization process that occurs at higher stresses. Further work on using an erosion chambers at high stresses is required to resolve this issue.

With the combined active layer formulation (Eq. (6)) the model is able to predict the sediment concentration boundary condition reasonably well for the first two high concentration events and subsequent DS events. However, during event HC3 the active layer model underpredicts the observed near bed concentrations (Fig. 5(a)). This is due to the relatively low wave stresses, combined with strong mean currents which tend to reduce near-bed concentrations by mixing sediment higher into the water column. This event also occurs immediately after the peak in Po discharge, thus there is probably a supply of new sediment which could be arriving at the 13 m as a wave-supported turbidity flow initiated in shallower water.

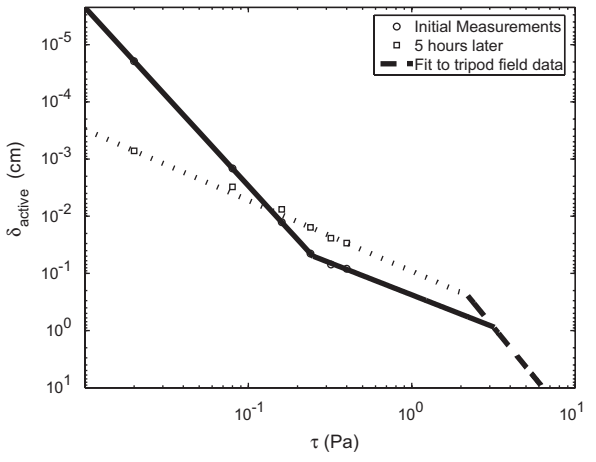

Fig. 6. Active layer depth (δ_{mix}) vs. τ. Solid line is the fit to initial measurements (circles) from an erosion chamber applied to a core immediately after the core was brought aboard the ship. Dotted line is the fit to erosion chamber measurements (squares) 5 h later. Dashed line represents the break in slope of (δ_{active}) vs. τ curve that is required to fit ABS near bed concentrations at high stresses.

4.3. Vertical 1D modeling of sediment concentration profiles

The sediment concentration profiles from the 1D model were compared to ABS-measured concentration profiles for the first high concentration event (HC1) and the second Bora-forced DS event (DS2) (Fig. 7). These events were chosen for detailed model-data comparison because they were the largest contributors to the flux for each transport process. In order to eliminate the errors associated with calibration of the ADCP sediment concentration estimates, the model-data comparison was only performed with ABS data. To calculate vertical profiles of concentration for each event the model was run with time varying input parameters over the duration of the event (gray shaded regions in Figs. 4 and 5) and then the model concentration profiles were temporally averaged. The ABS concentration profiles were averaged over the same time period for each event.

The model includes a correction for suspended sediment-induced density stratification that can be switched on or off (Wiberg and Smith, 1983). The active layer depth limitation on sediment availability can also be switched on or off. For HC1 without sediment density stratification turbulence damping, the model overpredicts the amount of sediment outside of the wave boundary layer by two orders of magnitude. Within the ~5 cm thick wave boundary layer, the concentration predictions of the model are roughly consistent with data. Adding an active layer limitation reduces the overall amount of sediment in suspension slightly but still grossly over-estimates the amount of sediment outside the wave boundary layer. When sediment density stratification is included, the model is able to predict the sharp drop-off in sediment concentration near the top of the wave boundary layer and bottom of the current boundary layer. The solution with sediment stratification and the active layer depth limitation (defined by Eq. (6)) is very similar to the solution with stratification and without the active layer depth limitation. Thus, the active layer depth limitation is not required to predict the concentration profile

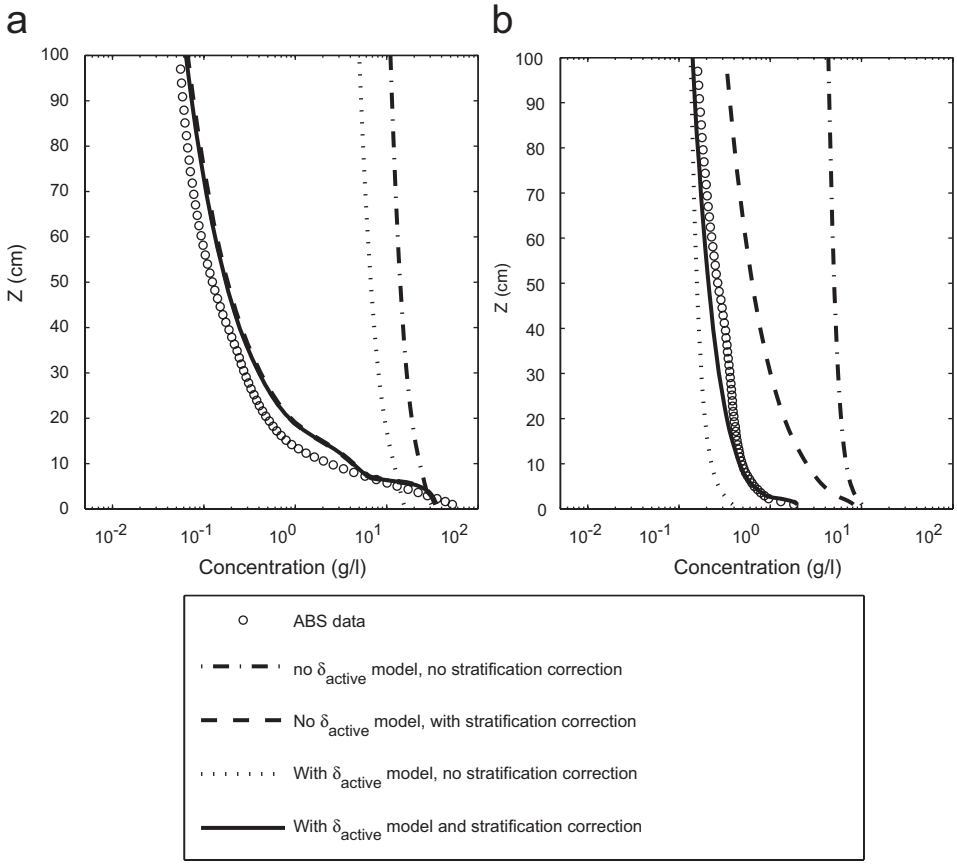

Fig. 7. ABS (open circles) and model sediment concentration profiles (line type as indicated in legend) for events (a) HC1 (b) DS2.

during the high concentration events, since the total volume resuspended during these events does not exceed the amount available from within the active layer depth.

With sediment stratification, the model predicts a dramatic shut down in turbulence at the top of the wave boundary layer, reducing the eddy diffusivity K_s for sediment from $3\,cm^2/s$ for the unstratified case to $\sim 0.1\,cm^2/s$ for the runs that include sediment stratification. The model shows a step-like structure where concentration is relatively uniform within the wave boundary layer, and exhibits a lutocline at the top of the wave boundary layer (Fig. 7(a)). The ABS data at 1 Hz also show this type of lutocline with a step-like structure; however, the lutocline in the ABS data is wavy with time scales similar to the interfacial gravity waves shown in Traykovski et al. (2000). The burst-averaged ABS concentration profile shown in Fig. 7(a) results in a smoother lutocline gradient, because the fluctuations of the lutocline are averaged. The lutocline in the model does not fluctuate on the wave time scale because the model does not resolve waves, thus the step-like structure is produced in the model output that would not be evident in the ABS profiles, which were averaged over a period of waves with similar properties. The fact that the sediment is limited to the wave boundary due to sediment-induced density stratification has important implications for the wave-supported turbidity flows. If this reduction in mixing did not occur, the sediment that was resuspended higher into the mean current boundary layer would be transported by the mean currents. With the shutdown of turbulence, the sediment remains in the wave boundary layer (60 g/l in the wave boundary layer vs. 0.05 g/l at 100 cmab) where mean currents are weak, and thus most of the transport occurs by gravitational forcing.

In contrast to the high concentration events, during Bora-forced DS conditions with stronger mean currents, sediment stratification is not as important. Instead, the suspended sediment bottom boundary condition becomes the limiting factor in controlling the model's ability to predict the concentration profile. The model run with no sediment stratification, no active layer depth limitation, and a reference concentration boundary condition (Eq. (5)), predicts a profile with concentrations that are one to two orders of magnitude greater than the measured values (Fig. 7(b)). Including sediment stratification, but no active layer depth limitation results in a profile with concentrations 2–3 times greater than the data. The predicted profile in this case also has a steeper vertical gradient, as the high concentrations allow greater sediment stratification. Including an active layer depth limitation, but not sediment stratification, results in a profile that has weaker vertical gradients than the data. This model under-predicts measured concentrations near the bed and over-predicts them above 100 cmab. Including both sediment stratification and a active layer depth limitation, which effectively limits resuspension at low stresses, results in a concentration profile that is consistent with the measured data. Thus, while in the high concentration case, stratification was important but an active layer depth limitation was not required, in this case with strong mean current forcing, both an active layer depth limitation and a stratification correction are required. The strong mean currents associated with Bora wind forcing conditions mixed greater concentrations to 100 cmab (0.150 g/l) than were present at that elevation during the high concentration events, even though the near-bed concentration during the DS events was more than an order of magnitude smaller. These higher concentrations well above the bed where the currents are strong result in the large fluxes observed during Bora-forced DS events.

5. Gravity flow modeling

5.1. Dynamics of wave-supported turbidity flows

Once the appropriate conditions occur for the formation of high sediment concentration layers within the wave boundary layer (high wave stresses with relatively low current stresses), the sediment will flow down-slope under the influence of gravity. The dynamics of these flows are controlled by the balance of gravitational forcing and friction from both the stationary sea floor and the overlying water. This balance is described by the linearized Chezy equation (Wright et al., 2001):

$$Hg' \sin\beta = C_d u_{grav} |u_{\max}|. \quad (7)$$

The left-hand side of Eq. (7) is the gravitational forcing term, where H is the thickness of the high concentration layer, g' is reduced gravity due to immersed weight of sediment in water and $\sin\beta$ is the seafloor slope. The right-hand side of the equation is the linearized frictional force, where the quadratic velocity term has been linearized to account for the wave velocities or along-shore

current velocities $\left(u_{\max}=\sqrt{u_{br}^2+u_{grav}^2+v_{curr}^2}\right)$ in the high concentration layer, which may be larger than the down-slope gravitational flow (Wright et al., 2001). Values for u_{max} and u_{grav} for the three wave-supported turbidity flow events are shown in Table 2. These values have been averaged over the duration of the event as indicated by the gray shading in Figs. 2 and 4. Interfacial friction between the moving high concentration layer and the overlying water column has been assumed to be much smaller than bed friction in this balance. This can be justified due the fact that if a high concentration layer is present there is not much mixing with the overlying flow. As flow velocities in the overlying water column increase the interfacial friction will increase, but the high concentration layer will also be mixed higher into the water column and will thus become a DS.

The parameters for the gravitational forcing term can be estimated from the ABS data. The height of the lutocline (H) is estimated by finding the maximum gradient in the 1-Hz-sampled ABS concentration profiles and then averaging this quantity over a burst. Profiles with maximum gradients less than 2 g/l/cm or profiles with maximum gradients within 1 cm of the bed are assigned a zero lutocline height. Typical lutocline gradients during the wave-supported turbidity flow events were around 10 g/l/cm. This technique produces lutocline heights that are similar to the 10 g/l thresholding method used in Traykovski et al. (2000), and profiles with maximum concentrations less than 10 g/l usually did not have a lutocline as defined by the 2 g/l/cm gradient threshold. Using the gradient or the thresholding method on burst-averaged ABS profiles results in an overestimate of lutocline height since the lutocline is a wavy surface. The lutocline height can be compared to estimates for wave boundary layer thickness based on the wave friction factor (Eq. (4)) as (Wiberg and Smith, 1983; Smith, 1977)

$$\delta_w=\sqrt{f_w/8}u_{br}/\omega_r. \tag{8}$$

As was found for high concentration layers on the Eel shelf (Traykovski et al., 2000) the wave boundary thickness is a good predictor of lutocline height (Fig. 8). During the three wave-supported turbidity flow events, the wave boundary layer and lutocline height ranged from 7 to 4 cm (Table 2). The depth-averaged reduced gravity for the three events can be calculated from the ABS concentration profiles by

$$g'=\frac{g(\rho_s-\rho_w)}{\rho_s\rho_w}\frac{1}{H}\int_0^H c(z)\,\mathrm{d}z, \tag{9}$$

where $c(z)$ is the mass concentration of sediment and ρ_s and ρ_w are sediment and water density. The seafloor slope ($\sin\beta$) at the Po 13-m tripod, based on bathymetry from Correggiari et al. (2001) was 0.002. The ratio of the gravitational forcing to the frictional velocity terms produces a similar C_d for the three events on the Po prodelta of approximately 0.0015. The force balance and drag coefficient are consistent to within 25% over almost one order of magnitude of stress (0.04–0.3 dyn/cm^2, equivalent to 0.004–0.03 Pa).

This can be compared to the force balance for the Eel shelf (Traykovski et al., 2000) to examine if the balances are similar at different locations. On the Eel shelf, the waves are larger, with 6–8 m significant heights vs. heights of 2–3 m at the Po site. The wave periods were also longer on the Eel shelf, with typical near-bed values around 14 s during storms vs. 8 s at the Po. The larger waves, longer periods and deeper observational site at the Eel resulted in 60 cm/s wave velocities at the Eel 60-m site vs.

Table 2
Parameters in wave-supported turbidity flow force balance

	Po prodelta, 13 m water depth (events HC1–HC3)	Eel Shelf, 60 m water depth
δ_w(cm)	7, 6, 4	12
g'(cm/s^2)	19, 12, 6	48
Sin β	0.002	0.005
U_{max} (cm/s)	45, 25, 15	60
U_{grav} (cm/s)	5, 4, 2	30
$Hg'\sin\beta$(cm^2/s^2)	0.27, 0.14, 0.048	2.9
$C_d u_{grav}\lvert u_{max}\rvert$(cm^2/s^2) based on $C_d=0.0015$	0.34, 0.16, 0.045	2.7
C_d (calculated from $Hg'\sin\beta/u_{grav}\lvert u_{max}\rvert$)	0.0012, 0.0014, 0.0016	0.0016

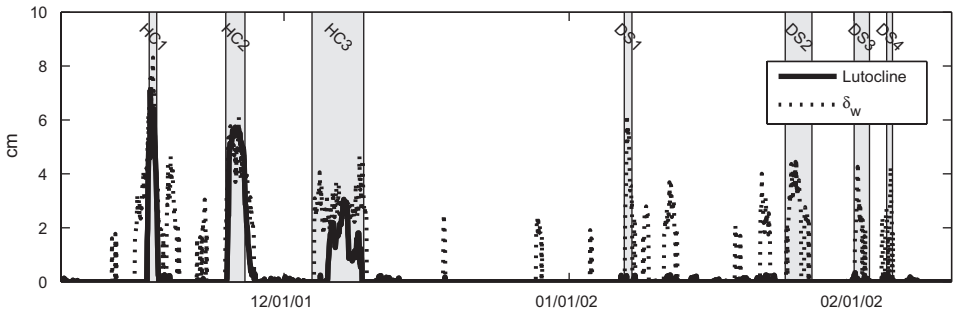

Fig. 8. Lutocline height (H) and wave boundary layer thickness (δ_w) time series.

15–45 cm/s at the Po 13-m site, and a wave boundary layer that was almost twice as thick on the Eel. As discussed previously, during the Eel observational study there was considerable uncertainty in the 2.5 MHz ABS derived-concentration estimates within the high concentration near-bed layers, and the sediment concentration in these layers was originally estimated conservatively at 20–80 g/l. Based on analysis of the Po data set this range may be a factor of two too low. For this force balance analysis, the depth-integrated concentration for the Eel is estimated as 80 g/l, the upper end of the original concentration estimates. This results in gravitational forcing of $\sim$3 dyn/cm^2 from the Eel study, an order of magnitude higher than the Po forcing. The drag coefficient estimated from the Eel data of $C_d \sim 0.0016$ is remarkably consistent with the Po data suggesting that the linearized Chezy force balance, ignoring interfacial friction with the overlying water column, holds over two orders of magnitude of forcing.

5.2. A 1D across-shelf gravity flow model

To compare of the location of wave-supported gravity-flows deposition on the Po prodelta to the Eel shelf, given the contrasting forcing conditions, a 1D, across-shelf numerical model was formulated. The model transports sediment across the shelf with a down-slope velocity determined by the linearized Chezy balance (Eq. (7)) as shown in Fig. 9. Sediment is input into the model on the inner shelf in depths shallower than 5 m. The model does not resolve the depth dependence of these flows. It assumes all of the sediment is contained within the wave boundary layer with a height of δ_w and there is no mixing of sediment into overlying waters. This allows the model to test depositional patterns due to only the wave-supported turbidity flows and is

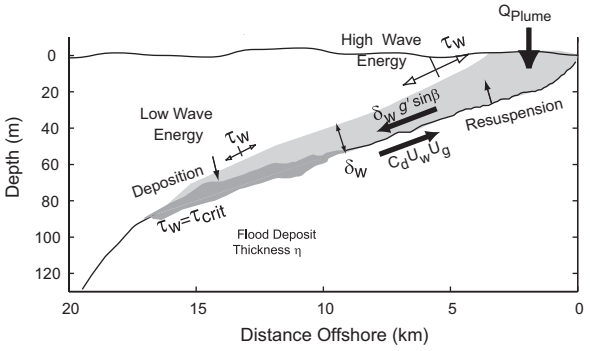

Fig. 9. Schematic of model domain showing a cross-shore transect of wave-supported turbidity flow processes.

approximately consistent with observations during periods of weak mean currents. The amount of sediment (C) in each across-shelf grid cell is determined by the sediment continuity equation, which balances erosion (E) and deposition (D) from the seabed and convergence of across shelf flux:

$$\frac{dC}{dt} = -\frac{du_{grav}C}{dx} - D + E. \quad (10)$$

Here C is the depth integrated wave boundary layer sediment concentration and is related to the depth-averaged sediment concentration (c) by $C = \delta_w c$. The thickness of the wave boundary layer is calculated by Eq. (8). The temporal evolution of the depositional patterns is calculated by the balance of erosion and deposition:

$$c_b \frac{d\eta}{dt} = D - E. \quad (11)$$

Here η is the thickness of the sediment deposit. Deposition is determined by settling flux ($D = w_s c$) and erosion is determined by an erosive flux. The erosive flux is limited by the reference concentration boundary condition and the amount of sediment

that is present on the seabed (i.e. E is set equal to the minimum of $w_e c_r$ and $c_b \eta / \mathrm{d}t$. The reference concentration (c_r) in the erosion boundary condition is determined by Eq. (5), and the erosional velocity (w_e) is equal to the particle settling rate (w_s) to balance depositional and erosive flux at a concentration equal to the reference concentration. This formulation allows mobile sediment to deposit and erode from an underlying fixed seabed. For this application of comparing the model to tripod time series, the predicted bathymetric changes are small thus the underlying bathymetry is not updated. The settling velocity is calculated using a hindered settling velocity formulation to account for the high concentrations present in the wave boundary layer:

$$w_s = w_{s0}\left(1 - \frac{C}{C_{gel}}\right)^m. \quad (12)$$

The fall velocity of the large flocs without hindered settling effects (w_{s0}) is estimated as 1.6 mm/s, and C_{gel}, the concentration at which the settling velocity goes to zero, is estimated as 160 g/l (Ross and Metha, 1989; Traykovski et al., 2004). The exponent m has a theoretical value of 5 and thus is not a fitting parameter (Ross and Metha, 1989). The erosion rate is controlled primarily by wave stresses (Eqs. (3) and (4)). These wave stresses decrease with increasing water depth as calculated by linear wave theory. Thus, sediment erosion occurs in shallow water where wave stresses are high; the sediment is then advected offshore via the gravity flows, and is deposited in deeper water where wave stresses are low. This model has similar dynamics to a model developed by Scully et al. (2003) with the primary difference being that their model assumes the sediment carrying capacity of the wave boundary layer is controlled by a critical Richardson number stratification limit, while the model in this paper parameterizes erosion and deposition as a function of bed stress and concentration. For the Eel shelf case, the two models produce similar results. The model presented in this paper also formed the conceptual basis for a including wave-supported gravitational sediment flows in a 3D circulation and sediment transport model (Harris et al., 2004, 2005).

This relatively simple model was run using wave conditions and bathymetry from the Eel river study to test the model (Fig. 10) and then applied to the Po prodelta to examine depositional patterns. The wave conditions and sediment input for the Eel shelf run were taken from a period from 12 to 21 January 1998, when a tripod similar the one used in the Po study was deployed on the 60-m isobath, 12 km north of the Eel River mouth. In the Eel shelf study, the sediment input was moderately well constrained with a rating curve for the Eel river and plume delivery characteristics based on the observations of Geyer et al. (2000). The depositional patterns immediately following flood events in 1995 and 1997 were well documented for the Eel flood events as several rapid response coring cruises were conducted. However, during 1998, when the tripod measurements of the wave-supported turbidity flow events occurred, a flood deposit was not measured by seabed observations. These constraints on the depositional patterns on the Eel shelf make it an excellent test case for this type of model. The model was then run with wave conditions and bathymetry from the Po prodelta site (Fig. 11). At the Po site, the sediment input was not as well known, as there were not observations of the plume during high flow events. However, observations of the depositional patterns immediately after a large Po flood event in 2000 were well constrained by seabed observations (Palinkas et al., 2005; Wheatcroft et al., 2006). Thus, in the Po case the model will be used to examine outputs of sediment distributions based on sediment inputs that are specified to match the observed flux.

5.3. *Across-shelf model runs for the Eel site and comparison to data*

For the Eel model runs the initial amount of resuspendable sediment on the seabed was not known; however, the subsequent sediment input from the Eel River was moderately well constrained. Because the river begins delivering sediment before the first peak in wave energy, the initial sediment supply was not expected to be a dominant variable, so it was assumed no preexisting sediment was available for transport. This results in a slight delay in the model prediction of the timing of the first wave-supported turbidity flow event relative to the data. Sediment input from the Eel River was added to the seafloor shoreward of the 40-m isobath (Fig. 10(b)) based on observations of sediment fallout from the coastally trapped plume (Geyer et al., 2000). In Geyer et al.'s work, the amount of sediment delivered to the cross-shelf transect 12 km north of the Eel river was determined by analysis of sediment and salinity observations and an Eel River rating curve developed by Morehead and Syvitski (1999).

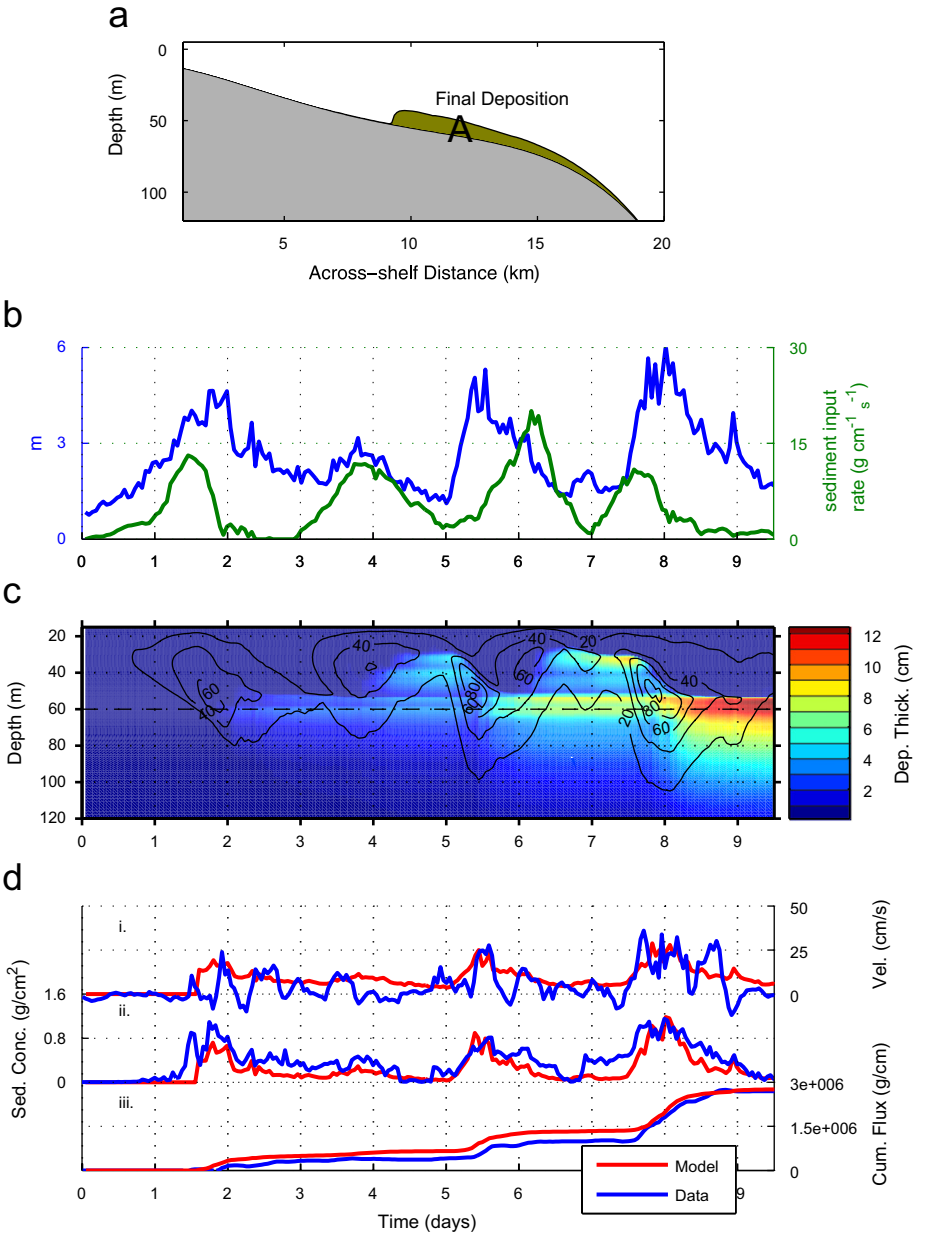

Fig. 10. Model runs for the Eel Shelf: (a) Bathymetry, initial and final across-shelf distribution of sediment deposition thickness. The vertical scale for the sediment deposition has been exaggerated by a factor of 100. The location of the tripod is indicated by A. (b) Wave height (left y-axis) and sediment input rate (right y-axis, proportional to river discharge). (c) Temporal and depth dependence of deposition (color scale) and suspended sediment concentration within the wave boundary layer (contours with units of g/l). A dashed line at 60 m depth depicts the tripod location. (d) Comparison of model results with tripod data from the 60 m isobath for (i) down-slope velocity, (ii) sediment concentration, and (iii) sediment flux.

During the observation period, the Eel River had four pulses of high flow associated with four wave events. Each pulse of high river flow results in a predicted peak in sediment concentration inshore of the 40 m isobath (see contours of sediment concentration in Fig. 10(c)). Transient deposition on the inner shelf is predicted after the second and third river pulses, as these pulses occur during low enough wave energy conditions so that the riverine sediment supply is greater than the offshore transport potential. The fourth pulse occurs during a period of high wave energy, and the sediment is

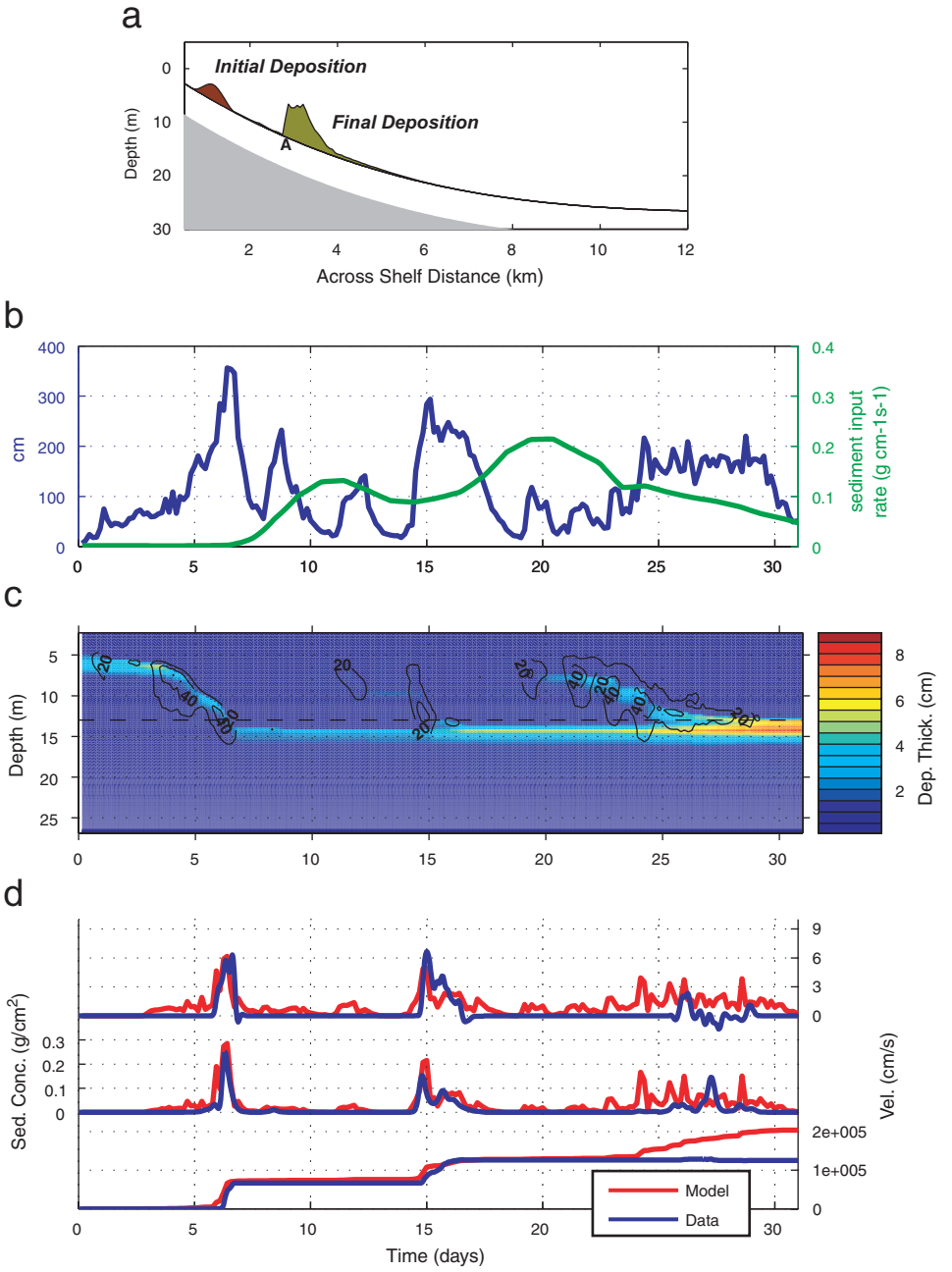

Fig. 11. Model runs for the Po prodelta: (a) Bathymetry, initial and final across-shelf distribution of sediment deposition thickness. The vertical scale for the sediment deposition has been exaggerated by a factor of 100. The location of the tripod is indicated by A. (b) Wave height (left y-axis) and sediment input rate (right y-axis, proportional to river discharge). (c) Temporal and depth dependence of deposition (color scale) and suspended sediment concentration within the wave boundary layer (contours with units of g/l). A dashed line at 13 m depth depicts the tripod location. (d) Comparison of model results with tripod data from the 13.5 m isobath for (i) down-slope velocity, (ii) sediment concentration, and (iii) sediment flux.

immediately advected offshore by the gravity flows. Each of the high wave events results in high near-bed concentrations at depths where there is sediment available to be resuspended. The highest concentrations occur between the 40 and 60 m isobath during the third and fourth wave events as sediment is resuspended from the transient inner shelf deposits and transported offshore via the

gravity flows. The outer edge of the deposition from the smaller first wave events occurs in slightly shallower water (45–80 m) than the deposition from the final two larger wave events (50–100 m, Fig. 10(c)).

The output of the model for down-slope velocity, wave boundary layer depth-integrated concentration, and cumulative flux was compared to observations from the 60-m tripod (Fig. 10(d)). The down-slope velocities predicted by the model and the observed peak down-slope velocities during each of the wave events have similar magnitudes of 20–30 cm/s. The observed down-slope flows have more temporal variability than the model, most of which is at tidal time scales. In the Eel study, the observed down-slope velocities were estimated by extrapolating velocity measurements at 100 and 30 cm above the seafloor to the top of the wave boundary layer in a manner similar to that described above for the Po data set. Because there are significant tidal velocities at these elevations, tidal variability is also evident in the down-slope velocity estimates. The model only accounts for gravitational flow, thus tidal variability is not predicted. The timing of the high concentration events are well predicted by the model owing to the correlation with wave forcing. The magnitude of the model depth-integrated concentration prediction is fairly consistent with observations after the original observed Eel concentration estimates are increased by a factor of two to account for acoustic attenuation as discussed earlier. Increasing, the observed concentration estimates also results in a good match between predicted and observed cumulative flux. The deposition of 10–15 cm at the 60-m isobath is also consistent with acoustic bed elevation measurements during this period. This amount of deposition at the 60 m isobath is also consistent with modeling results of Scully et al. (2002) and Scully et al. (2003). The predicted location of the deposit between 50 and 100 m water depths for this 1998 data set is consistent with the location of flood deposits measured by seabed observations after major Eel River flood events during the winters of 1995 and 1997. Seabed sampling in March of 1998 did not reveal a measurable flood deposit (Wheatcroft and Borgeld, 2000). However, this seabed sampling occurred several months after the 1998 depositional events and subsequent erosional events were observed in the ABS time series before the seabed sampling cruises (Traykovski et al., 2000). These erosional events may have resuspended the sediment in the wave-supported turbidity flow deposit before the seabed sampling cruise in 1998.

5.4. Across-shelf model runs for the Po Site and comparison to data

In the Po model runs, the initial seabed conditions prior to the period of high river input are critical, since the first wave-supported turbidity flow event occurs before river discharge begins to increase. During this first event the wave energy is sufficient to transport more sediment than is available from the seabed, thus sediment input constraints are required for the model to predict flux estimates that are consistent with the data. The active layer formulation alone is insufficient to limit the amount of sediment that would pass the 13 m isobath observational site if a large supply of sediment were available on the inner shelf at the start of the model run. Therefore, the initial distribution of sediment was adjusted to predict a flux consistent with the observations for the first event (Fig. 11(a)). With a flux that is consistent with the observations, the model predicts deposition to occur in 14–17 m water depths for the first event.

For the subsequent events during the period of high river outflow, the initial distribution is less important because all of the initially available sediment is transported offshore during the first event. In the second wave-supported turbidity flow event the amount of wave energy is the limiting factor in the across-shelf transport. A sensitivity analysis conducted by varying the amount of riverine sediment input into the model revealed that increasing the amount of sediment input into the model due to delivery from the Po River beyond the minimum required to predict the observed flux at the 13 m isobath does not further increase the amount of sediment transported across-shelf. The temporal dependence of the sediment input (Q_s) was related to the Po water discharge (Q) by $Q_s = AQ^{2.3}$ based on Kettner and Syvitski (in press), and new river sediment was introduced into the model inshore of the 8 m isobath. It was found that as long as the constant A was large enough to deliver 0.16 g/cm/s during the second event then wave energy would limit the flux past the 13-m isobath to an amount consistent with observations. Increasing the riverine input beyond this amount resulted in additional deposition inshore of the 13-m isobath. For the minimum value of A required to match the flux observations at 13 m, almost all the

sediment deposited from the river was transported offshore of 13 m and deposited in 14–17 m water depths, similar to the first event.

In the third high wave energy event (model days 24–29), just after the peak in river discharge, the observations show a brief period of gravity flow while the model predicts a longer duration of gravity flow (Fig. 11(d)). The model predicts a gravity flow during the entire 5-day period of elevated wave energy, which results in a significant flux of sediment past the 13-m isobath. The observations show no net offshore flux during this period because the down-slope velocity pulse associated with the gravity flow occurs before the peak in concentration. As was shown in Figs. 3 and 4, although there is a weak gravity flow velocity pulse during this event, the flux is controlled primarily by ambient overlying currents and not by gravity-flow forcing. Since the model does not account for overlying current forcing, it fails to predict the flux direction and magnitude correctly for this event.

Unlike the Eel 60-m data, the seabed elevation time series from the 13 and 20-m isobath ABS data shows no net elevation changes during the gravity flows on the Po prodelta. The model shows 6 cm of deposition at the 13-m isobath due entirely to the third event, during which the model failed due to forcing from overlying currents. If this event is not included, the model predicts deposition to occur at depths between 14 and 17 m, which is not inconsistent with the tripod data that shows no deposition at the 13 and 20-m isobaths. Unfortunately, seabed observations were not taken immediately after the November–December 2002 Po flood events. A seabed coring survey, conducted in February of 2003, did not reveal a distinct flood deposit that could be related to gravity flows at depths of 10–20 m (Wheatcroft, pers. comm., 2005). However, as documented is this paper, there were several large, Bora-forced, downcoast sediment transport events after the gravity flow events, and before the February 2003 seafloor sampling cruises, that could have eroded the flood deposits. A coring survey taken in December 2000 after the large ($9650\,m^3/s$) Po flood event of October 2000 revealed a distinct flood deposit (Palinkas et al., 2005; Wheatcroft et al., 2006). Based on resistivity profiles and X-radiograph imagery (Wheatcroft et al.'s Fig. 7, 2006), the thickest sediment deposits (20–36-cm thick) associated with this flood event were located in four main lobes associated with the Po distributaries, one of which was centered approximately on our 13-m tripod site. These main lobes had maximum depositional thickness in 8–12 m water depth. Most of the deposition was located inshore of the 15 m isobath; however, in two locations the deposits extend into deeper waters. In front of the Pila distributary, where the seafloor slope is steepest and wave-supported turbidity flows are most likely to occur, the deposits extend to 25–28 m water depths. At our tripod site, where wave-supported turbidity flows were observed 2 years later, the deposits extended into water depths of 20–22 m. Either of these lobes could potentially be related to gravity flows, as there was a 24-h period of 3.7 m significant wave height and an 8-day period of 2-m significant wave height after the peak of the 2000 flood event and before the coring survey. Wheatcroft et al. (2006) suggest there is sedimentary evidence for gravity flow emplacement in a core taken from the 20 m isobath near the Pila distributary. Since detailed observations of the hydrodynamic structure and sediment fallout rates from the Po's distributary plumes during flood conditions were not conducted as part of this study, modeling studies may be the best approach to determine the role of gravity flows vs. direct deposition from the buoyant surface plume in emplacing the deposits observed during the 2000 flood events (Friedrichs and Scully, 2007).

6. Conclusions

Observations of sediment transport processes on the Po prodelta have shown that wave-supported turbidity flows occurred during periods of high wave energy. The periods of high wave energy associated with wave-supported turbidity flows occurred *before* and during a period of high river discharge. The observation of a wave-supported turbidity flow before the period of high discharge shows that these flows can be generated by resuspension of sediment on the seafloor and do not exclusively occur when sediment is actively entering the system.

The kinematics of these flows appear similar to those observed on the Eel shelf, in that the thickness of the high concentration layer scales with the wave boundary layer thickness, and offshore flow is observed within tens of centimeters of the seafloor with onshore or weak flow above. The dynamics of these flows are also similar to those observed on the Eel, with the force balance between down-slope

gravitational forcing and frictional drag remaining relatively consistent over two orders of magnitude of force. This dynamic similarity allows the flux associated with these flows to be described relatively successfully using a simple 1D across-shelf model. However, the details of the formulation of the bottom boundary condition are very important to fit the data accurately. Here a traditional reference concentration bottom boundary condition was combined with a sediment mixing-depth formulation to limit the amount sediment in suspension. The reference concentration boundary condition alone would allow far too much sediment to be resuspended at moderate stresses.

The across-shelf modeling of the wave-supported turbidity flows reveals how both wave energy and sediment supply limitation can constrain the amount of sediment transported across-shelf by wave-supported turbidity flows. In the first event on the Po prodelta and the fourth event on the Eel shelf, the waves were energetic enough to transport more sediment than was available from the bed, thus sediment availability constrained the amount of across-shelf transport. In the second Po prodelta event and the second and third Eel shelf events, the wave energy (and timing relative to river discharge) was potentially insufficient to transport the available sediment across the shelf thus transient inner-shelf deposits formed. This type of simple flux model provides a useful tool to examine flux potential as a function of river input and wave energy, and to examine resulting depositional patterns.

As opposed to the Eel shelf, on the Po prodelta, wave-supported turbidity flows were not the dominant transport mechanism at the observational site. Southerly mean current events forced by Bora winds from the northeast transported far more sediment south than was transported offshore by the wave-supported turbidity flows. This difference occurs in part because the wave-supported turbidity flows on the Po are thinner and lower concentration than those on the Eel and because the observational site on the Po has a lower slope. In addition, the mean current-forced transport events at the Po site also have a consistent southerly direction due to the Bora wind forcing, as opposed to the Eel shelf where flux direction varies throughout the year due to northerly and southerly forcing. However, closer to the main Pila distributary of the Po River, wave-supported turbidity flows have the potential to move sediment into deeper water, where it is less likely to be resuspended and transported south. Thus, wave-supported turbidity flows could potentially enhance preservation of sediment on the prodelta, leading to a faster progradation rate than would occur without this mechanism. Additional modeling work that includes both transport mechanisms (such as that performed in Harris et al., 2004, 2005) would be necessary to investigate the role of wave-supported turbidity flows in contributing to the growth of the Po delta.

Acknowledgements

The authors would like to thank Jay Sisson and Glenn McDonald whose diving skills were invaluable during the turn-around and recovery cruises. We thank the crews aboard the R/V *Garcia del Cid*, and R/V *Seward Johnson II* and colleagues in Italy, Spain, who provided facilities to make this work feasible, particularly Stefano Miserocchi, Fabio Trincardi, Annamaria Correggiari and Pere Puig. P. Traykovski and R. Geyer were funded by the US Office of Naval Research under Grant No. #N00014-02-10378, and P. Wiberg was funded under Office of Naval Research under Grant No. #N00014-02-10369; both under the direction of program manager, Tom Drake. This is Woods Hole Oceanographic Institution contribution No. 11286.

References

Artegiani, A., Bregant, D., Paschini, E., Pinardi, N., Raicich, F., Russo, A., 1997. The Adriatic Sea general circulation. Part II: baroclinic circulation structure. Journal of Physical Oceanography 27, 1515–1532.

Bondesan, M., 2000. Guida all escursione nel delta del Po. Le pianure conoscenza e salvaguardia il contributo delle scienze della terra. Atti del convegno. Regione Emilia-Romagna, Italia, pp. 381–393 (English translation available at: 〈http://www.regione.emilia-romagna.it/geologia/econv_pia.htm〉).

Cattaneo, A., Correggiari, A., Langone, L., Trincardi, F., 2003. The late-Holocene Gargano subaqueous delta, Adriatic shelf: sediment pathways and supply fluctuations. Marine Geology 193 (1–2,15), 61–91.

Correggiari, A., Trincardi, F., Langone, L., Roveri, M., 2001. Styles of failure in heavily-sedimented highstand prodelta wedges on the Adriatic shelf. Journal of Sedimentary Research 71, 218–236.

Deines, K.L., 1999. Backscatter estimation using broadband acoustic Doppler current profilers. In: Oceans 99 MTS/IEEE Conference Proceedings, 13–16 September, or RD Instruments application note: 〈http://www.rdinstruments.com/rr/reports/echopaper.doc〉.

Dietrich, W.E., 1983. Settling velocity of natural particles. Water Resources Research 18, 1615–1626.

Fredsøe, J., Deigaard, R., 1992. Mechanics of Coastal Sediment Transport. World Scientific, New Jersey, 369pp.

Friedrichs, C.T., Scully, M.E., 2007. Modeling deposition by wave-supported gravity flows on the Po River prodelta: from seasonal floods to prograding clinoforms. Continental Shelf Research 27, 322–337.

Friedrichs, C.T., Wright, L.D., 2004. Gravity-driven sediment transport on the continental shelf: implications for equilibrium profiles near river mouths. Coastal Engineering 51, 795–811.

Fox, J.M., Hill, P.S., Milligan, T.G., Boldrin, A., 2004. Flocculation and sedimentation on the Po River delta. Marine Geology 203, 95–107.

Geyer, W.R., Hill, P., Milligan, T., Traykovski, P., 2000. The structure of the Eel River plume during floods. Continental Shelf Research 20, 2067–2093.

Harris, C.K., Traykovski, P.A., Geyer, R.W., 2004. Including a near-bed turbid layer in a three-dimensional sediment transport model with application to the Eel River Shelf, Northern California. In: Spaulding, M. (Ed.), Proceedings of the Eighth Conference on Estuarine and Coastal Modeling, ASCE, pp. 784–803.

Harris, C.K., Traykovski, P.A., Geyer, R.W., 2005. Flood dispersal and deposition by near-bed gravitational flows and oceanographic transport: a numerical modeling study of the Eel River shelf, northern California. Journal of Geophysical Research 110, 16.

Hill, P.S., Milligan, T.G., Geyer, W.R., 2000. Controls on effective settling velocity of suspended sediment in the Eel River flood plume. Continental Shelf Research 20, 2095–2112.

Hill, P.S., Fox, J.M., Crockett, J., Curran, K.J., Drake, D.E., Friedrichs, C.T., Geyer, W.R., Milligan, T.G., Ogston, A.S., Puig, P., Scully, M.E., Traykovski, P., Wheatcroft, R.A., in press. Sediment delivery to the seabed on the Eel River continental margin. In: Nittrouer, C.A., Austin, J.A., Jr., Field, M.E., Kravitz, J.H., Syvitski, J.P.M., Wiberg, P.L. (Eds.), IAS Special Publication 37, Continental-margin sedimentation: From sediment transport to sequence stratigraphy. Blackwell Publishing Ltd, Oxford (in press, December 2006).

Kettner, A.J., Syvitski, J.P.M., in press. Predicting discharge and sediment flux of the Po River, Italy since the Late Glacial Maximum. IAS (special issue).

Lee, T.H., Hanes, D.M., 1995. Explicit solution to the acoustic backscatter equation to measure the concentration of uniform, suspended particles. Journal of Geophysical Research 100 (C2), 2649–2657.

Lynch, J.F., Irish, J.D., Sherwood, C.R., Agrawal, Y.C., 1994. Determining suspended particle size information from acoustical and optical backscatter measurements. Continental Shelf Research 14 (10–11), 1139–1164.

Madsen, O.S., 1994. Spectral wave–current bottom boundary layer flows. Coastal Engineering 1994. In: Proceedings of the 24th International Conference, Coastal Engineering Research Council/ASCE, pp. 384–398.

Middleton, G.V., 1993. Sediment deposition from turbidity currents. Annual Review of Earth and Planetary Science 21, 89–144.

Miller, M.C., McCave, I.N., Komar, P.D., 1977. Threshold of motion under unidirectional currents. Sedimentology 24, 507–527.

Milliman, J.D., Meade, R.H., 1983. World-wide delivery of river sediment to the oceans. Journal of Geology 91, 1–21.

Morehead, M.D., Syvitski, J.P., 1999. River Plume sedimentation modeling for sequence stratigraphy: application to the Eel Margin, northern California. Marine Geology 154, 29–41.

Moore, D.G., 1969. Reflection profiling studies of the California Continental Borderland: structure and quaternary Turbidite Basins. Geological Society of America, Special Paper 107, 142.

Nelson, 1970. Hydrography, sediment dispersal, and recent historical development of the Po River Delta, Italy. In: Morgan, J.P. (Ed.), Deltaic Sedimentation, Modern and Ancient. Soc. Econ. Paleontol. Mineral. Special Publication 15, pp. 152–184.

Nittrouer, C.A., Miserocchi, S., Trincardi, F., 2004. The PASTA project: investigation of Po and Apennine Sediment transport and accumulation. Oceanography 17 (4), 46–57.

Palinkas, C.M., Nittrouer, C.A., Wheatcroft, R.A., Langone, L., 2005. The use of ^{7}Be to identify vent and seasonal sedimentation near the Po River delta, Adriatic Sea. Marine Geology 222–223, 95–112.

Ross, M.R., Metha, A.J., 1989. On the mechanics of lutoclines and fluid mud. Journal of Coastal Research 5, 51–61.

Scully, M.E., Friedrichs, C.T., Wright, L.D., 2002. Application of an analytical model of critically stratified gravity-driven sediment transport and deposition to observations from the Eel River continental shelf, northern California. Continental Shelf Research 22, 1951–1974.

Scully, M.E., Friedrichs, C.T., Wright, L.D., 2003. Numerical modeling results of gravity-driven sediment transport and deposition on an energetic continental shelf: Eel River, northern California. Journal of Geophysical Research 108(C4), 17-1–17-14.

Sherwood, C.R., Carniel, S., Cavaleri, L., Chiggiato, J., Da, H., Doyle, J.D., Harris, C.K., Niedoroda, A.W., Pullen, J., Reed, C.W., Russo, A., Sclavo, M., Signell, R.P., Traykovski, P., Warner, J.C., 2004. Sediment dynamics in the Adriatic Sea investigated with coupled models. Oceanography 17 (4).

Smith, J.D., Mclean, J.R., 1977. Spatially averaged flow over a wavy surface. Journal of Geophysical Research 82, 1735–1746.

Stevens, A.W., Wheatcroft, R.A., Wiberg, P.L., 2007. Seabed properties and sediment erodibility along the western Adriatic margin, Italy. Continental Shelf Research 27, 400–416.

Thorne, P.D., 1993. Analysis of acoustic measurements of suspended sediments. Journal of Geophysical Research 98, 899–910.

Traykovski, P., Geyer, W.R., Irish, J.D., Lynch, J.F., 2000. The role of wave-induced density-driven fluid mud flows for cross-shelf transport on the Eel River continental shelf. Continental Shelf Research 20, 2113–2140.

Traykovski, P., Geyer, R., Sommerfield, C., 2004. Rapid sediment deposition and fine-scale strata formation in the Hudson estuary. Journal of Geophysical Research 109, F02004.

Trincardi, F., Correggiari, A., Roveri, M., 1994. Late Quaternary transgressive erosion and deposition in a modern epicontinental shelf: the Adriatic semienclosed basin. Geo-Marine Letters 14, 41–51.

Wheatcroft, R.W., Borgeld, J.C., 2000. Oceanic flood deposits on the northern California shelf: large-scale distribution and

small scale physical properties. Continental Shelf Research 20, 2163–2190.

Wheatcroft, R.W., Borgeld, J.C., Born, R.S., Leithold, E.L., Nittrouer, C.A., Sommerfield, C.K., 1996. The anatomy of an oceanic flood deposit. Oceanography 9 (3), 158–162.

Wheatcroft, R.W., Sommerfield, C.K., Drake, D.E., Borgeld, J.C., Nittrouer, C.A., 1997. Rapid and widespread dispersal of flood sediment on the northern California margin. Geology 254 (2), 163–166.

Wheatcroft, R.A., Stevens, A.W., Hunt, L.M., Milligan, T.G., 2006. The large-scale distribution and internal geometry of the fall 2000 Po River flood deposit: Evidence from digital X-radiography. Continental Shelf Research 26, 499–516.

Wiberg, P., Smith, J.D., 1983. A comparison of field data and theoretical models for wave–current interactions at the bed on the continental shelf. Continental Shelf Research 2 (2–3), 147–162.

Wiberg, P.L., Drake, D.E., Cacchione, D.A., 1994. Sediment resuspension and bed armoring during high bottom stress events on the northern California continental shelf: measurements and predictions. Continental Shelf Research 14, 1191–1219.

Wright, L.D., Friedrichs, C.T., Kim, S.C., Scully, M.E., 2001. The effects of ambient currents and waves on gravity-driven sediment transport on continental shelves. Marine Geology 175, 25–45.